This unedited manuscript has been accepted for publication in Biophysical Journal and is freely available on BioFast at http://www.biophysj.org. The final copyedited version of the paper may be found at http://www.biophysj.org.

Strain-dependent kinetics of the myosin working stroke, and how they could be probed with optical-trap experiments.

David Smith* and John Sleep[+]

** Dept. of Physiology, Monash University, Clayton, Victoria 3800, Australia,*
[+] Randall Centre, King's College London, London SE1 1UL, U.K.

ABSTRACT: The strain-dependent kinetics of the myosin working stroke under load is derived from a flat-energy-landscape model for its untethered lever-arm, and compared with other scenarios in the literature. The 'flat-landscape' scenario is compatible with muscle-fibre experiments, but is more critically relevant to single-myosin experiments with an optically-trapped actin filament. In such experiments, the strain-dependence of stroke kinetics may be explored by comparing event-averaged and time-averaged displacements of the filament. With a specific kinetic model of the crossbridge cycle, we have previously shown that the event-averaged displacement underestimates the working stroke. Here we predict that the two kinds of averaging give diverging estimates of the working stroke as the resolving time of the event detector is decreased to 1ms or less, the discrepancy being critically dependent on the strain-dependence of the stroke rate. Such analysis of trap displacement data offers the possibility of testing the strain-dependent stroke rate predicted by the flat-landscape model.

Running title: Kinetics of the myosin working stroke….
Keywords: myosin, stroke, kinetics, strain, traps

* To whom reprint requests should be addressed. Email: david.smith@med.monash.edu.au

INTRODUCTION

It is generally believed that myosin makes force and movement in muscle by a working stroke when bound to actin; the kinetics of this transition is governed by the difference in elastic strain energies of the initial and final states and therefore depends on the initial strain. In this paper we suggest how the kinetics of the stroke can be explored with optical-trap experiments.

To this end, we first derive expressions for the rate constants from the reaction-energy profile first suggested by Huxley and Simmons (1), which is broadly consistent with the atomic structures of myosin with stereospecific positions of its neck region for pre-stroke and post-stroke states (2-4). In the absence of a load, the lever-arm is assumed to swing freely on a flat energy plateau between sharp potential wells for the pre-stroke and post-stroke states. Under isometric conditions, where the distal end of the neck and the actin filament are both held fixed, the stroke may be inhibited by the energy cost of bending the lever, and the plateau region becomes a parabolic function of lever-arm orientation, the angle of minimum energy being determined by the position of the tethering point. The strain-dependent stroke rate of this 'flat-landscape' model is then calculated from Kramers' theory of unimolecular reactions in the limit of overdamping. Other scenarios, in which all strain-dependence has been assigned to the forward or the backward rate, have been used as discussed below. All scenarios must comply with the strain-dependent equilibrium constant of the stroke transition prescribed by the change in strain energy.

Turning now to single-myosin experiments with an optically-trapped actin filament, we have shown previously (5) that the determination of the working stroke from these experiments is complicated by strain-dependent mechanochemistry. A statistical treatment is necessary because the pre-stroke bound state is not observed in non-processive myosins such as myosin II. The conventional method of analysis uses the event-averaged displacement of the actin filament, which is the unweighted average of the mean displacements in each period of attachment following a binding event (6,7): after a small correction for the stiffness of the traps, this mean displacement is equated with the working stroke. This result is expected if the myosin always makes a stroke, or strokes with the same probability, after binding to different sites on the actin, in which case the forward stroke rate must be strain-independent. This assumption is contra-indicated by length-step experiments in the muscle fibre, where the rate of phase-2 tension recovery is a strongly decreasing function of the size of the step (1,8); this recovery has been modelled by putting all the strain-dependence in the forward rate. Thus it is desirable to have a first-principles model of the kinetics of the working stroke.

To establish terminology, it is convenient to use the same kinetic scheme throughout for actin-myosin-nucleotide states, namely

$$1 \underset{k_{-1}(x)}{\overset{k_1(x)}{\rightleftharpoons}} 2 \underset{k_{-2}(x)}{\overset{k_2(x)}{\rightleftharpoons}} 3 \underset{k_{-3}}{\overset{k_3}{\rightleftharpoons}} 4 \xrightarrow{g} 1$$

Scheme 1

where state 1 is M.ADP.Pi, 2 and 3 are the pre-stroke and post-stroke A.M.ADP.Pi states, and state 4 is the rigor state A.M. The detachment step 4→1 requires ATP binding. For simplicity, A.M.ADP states and states with bound ATP are omitted. This omission is justified for trap experiments at micromolar levels of ATP.

This scheme has been analyzed for application to low-frequency trap data (5), where the minimum duration between detectable events (minimum resolving time) is ≥ 5 ms. The event-

averaged mean displacement was predicted by assuming that the only detectable bound state was the rigor state A.M. Under these conditions, the event-averaged displacement is controlled by the strain-dependent equilibrium constant of the stroke, not the rate constants of the forward and backward transitions. Testing this model is difficult because the predicted deflation factor (mean bound-state displacement/working stroke) varies substantially with kinetic parameters such as the equilibrium constant of the stroke and the rate of pre-stroke detachment from actin, which are not under experimental control. Consequently, the observed mean displacement is a lower bound for the working stroke. In the discussion section, we suggest ways around this problem.

High-frequency trap data, in which the minimum resolving time is $\leq 1\,\mathrm{ms}$, should reveal the initial short-lived post-stroke state A.M.ADP.Pi as well as the downstream states A.M.ADP and A.M, but there appears to be no obvious way of detecting the former if no additional stroke is associated with the release of phosphate. A possible handle for this problem is the use of two types of averaging in analyzing displacement data. The conventional method uses event-averaging, which assigns unit weight to each binding event: one can also construct the time-averaged displacement, which assigns unit weight to each displacement in a uniformly-sampled time recording. The fundamental significance of time averaging is that, under equilibrium conditions when the ergodic theorem applies, time averaging is equivalent to ensemble averaging as used in statistical mechanics. Note that time averaging is equivalent to a weighted form of event averaging where the mean displacement in each period of attachment is weighted by its lifetime, provided that the mean displacement in detached periods is zero. If the lifetime of the detected bound states is strain-independent, as for A.M in Scheme 1, then the same lifetime applies to all actin sites and the two averaging methods give the same result. At higher time resolution where the A.M.ADP.Pi state is detected, the two averages are not expected to be the same because the lifetime of this state depends on the rate of stroke reversal, which can be strain-dependent. Thus different scenarios for the strain-dependence of the stroke rate control the difference between event-averaged and time-averaged displacements in high-frequency data, even though the ratio of the strain-dependent forward and backward rates is determined from detailed balancing. Using both kinds of averaging should give information on the strain-dependence of stroke kinetics, and also shed more light on the relation between these average displacements and the true working stroke.

To demonstrate these relationships, event-averaged and time-averaged mean displacements have been calculated from Scheme 1 as a function of different kinetic scenarios and the time resolution of the event detector. For high-frequency data, these average displacements are numerically different, the difference being an increasing function of how much of the strain-dependence of stroke equilibrium is assigned to the rate of stroke reversal. As detection is degraded by increasing the resolving time of the event detector, this difference reduces smoothly to zero for resolving times above 5 ms where the influence of the strain-dependent lifetime of the A.M.ADP.Pi state is negligible, as modelled previously.

To apply stroke-kinetic scenarios to trap data, consider how actomyosin transition rates are affected when the actin filament is weakly tethered by the traps. In this case, working-stroke events are far from isometric; as the lever arm swings, the actin-beads dumbbell is pulled smoothly out of the traps and any large strain-energy barrier associated with the isometric transition is avoided. To analyse this effect, note that the working stroke is driven not only by thermal fluctuations in the myosin but also by thermally-generated displacement fluctuations of the actin-beads assembly. The effective stroke rate then depends on the relative time scales of filament fluctuations and the stroke. If filament fluctuations are more rapid than the working stroke, the initial distribution of displacements is in Boltzmann-equilibrium; we then show that the stroke rate is obtained from its isometric form by replacing myosin stiffness by the stiffness of myosin and the traps connected in series. This limit is

realized experimentally; the damping frequency of the actin-beads 'dumbbell' with myosin bound is of the order of $10^5 s^{-1}$, whereas the fastest measured stroke rate is under $10^4 s^{-1}$.

The above 'Brownian-averaged' reaction rates are then applied to kinetic models of trap displacement data. With high-frequency data, the event-averaged mean displacement is controlled by the strain-dependence of the stroke rate, and a model with binding and stroke transitions is sufficient. Predictions at finite time resolution are made using Scheme 1, by inserting the probability that the lifetime of the post-stroke states exceeds the resolving time.

THE STROKE RATE OF THE FLAT-LANDSCAPE MODEL

In this section the strain-dependent rate constant of the working stroke is calculated from the reaction-energy profile of the flat-landscape model. Evidence for this model derives from known atomic structures of myosin-ligand complexes. The crystallized post-stroke state was the near-rigor state A.M.ADP (2). Under ATP-cycling conditions, the pre-stroke state is the products state A.M.ADP.Pi which readily releases the products of hydrolysis, so a vanadate analogue was used for crystallization (3). In these two states, the orientations of the neck region of the myosin heavy chain are stable, at 110^o and 40^o respectively to the plus-end of the actin filament; these observations are consistent with those obtained from cryo-EM in insect flight muscle (4), and spin-label and fluorescent probes (9,10). Between these states, the C-terminus of the neck region is displaced by 10-11nm. A recent molecular-dynamics simulation of the return stroke (11) suggests that the neck region of detached myosin does swing freely between these limits, thus acting as a lever arm. This lever arm, including its converter connection to the motor domain, exhibits elastic compliance and bends by 2nm under isometric tension in the muscle fibre (12). This compliance may be distributed along the lever-arm, but there is evidence that at least part of it is localized in the converter (13).

The flat-landscape model is summarized in Figure 1. If the distal end of the lever-arm is unconstrained, the lever-arm swings on a flat energy surface $G_B(\theta)$ between the orientational potential wells of the pre-stroke and post-stroke states, at angles θ_2 and θ_3. This situation is almost realized for myosin-S1 bound to a weakly-trapped actin filament, as in the three-bead trap experiment. Weak restoring forces generated by the traps allow large-scale movements of the actin-beads 'dumbbell' relative to the tethered myosin; nevertheless, there will be a small additional energy cost to the stroke reaction when the stroke pulls the dumbbell out of the traps. In striated muscle, the positional constraints are much stronger and limited by the elasticity of the filaments.

It is convenient to calculate the stroke rate under isometric conditions, where the actin filament and the C-terminus of the neck region are held fixed. In this case the bound myosin must stroke against the elastic energy of its own deformation, commonly assumed to be a bending of the lever arm. The energy cost will be considerably in excess of thermal energy unless the lever-arm is initially bent in the opposite direction, in which case that strain would be relieved by the stroke (Figure 1B). Let x be the longitudinal distance from myosin to actin site, such that x is also the bending strain of the bound myosin in its pre-stroke state. Then the Gibbs energy is $G(x,\theta) = G_B(\theta) + V(x,\theta)$ where $V(x,\theta) = \frac{1}{2}k\{x + R(\cos\theta - \cos\theta_2)\}^2$ for bending stiffness k, and the working stroke is $h \equiv R(\cos\theta_3 - \cos\theta_2)$ where R is the length of the lever-arm. The strain energies of the initial and final states are $\frac{1}{2}kx^2$ and $\frac{1}{2}k(x+h)^2$, which differ by $kh(x + h/2)$; thus the working stroke is energetically favourable when $x < -h/2$, and subject to an extra energy barrier of this amount when $x > -h/2$. If the reaction rate is limited only by the highest energy in the pathway, then the isometric stroke rate as a function of x would in the first case be flat, and in the second case reduced by the

factor $\exp(-\beta kh(x+h/2))$ where $\beta = 1/k_{\mathrm{B}}T$. Rates of tension recovery in fibres after a length step can be reproduced in this way (14,15).

However, the above result cannot be used under trap conditions, which are far from isometric. When the stroke pulls the actin filament out of the traps, the highest strain-energy barrier barely exceeds thermal energy and the 'highest-energy-barrier' approximation breaks down. Then a more sophisticated kinetic model is required. In the next subsection, the isometric stroke rate is calculated from first principles, giving a formula valid for all positive values of *k*. With this result to hand, the kinetics of the working stroke can be derived under conditions of weak elastic tethering, as required for analysing weak-trap displacement data.

The flat-landscape model of the working stroke exhibits inversion symmetry between the forward and backward transitions, but at different values of the pre-stroke strain. Mathematically, $V(x,\theta) = V(x',\theta')$ where $x' = -x-h$ and $\cos\theta_3 - \cos\theta' = \cos\theta - \cos\theta_2$. This symmetry is reflected in the kinetics: $k_{-2}(-x-h) \equiv Ck_2(x)$ where C is a constant. Detailed balancing in the form $k_2(x)/k_{-2}(x) \equiv K_2 \exp(-\beta kh(x+h/2))$ can be used to eliminate the backward rate, giving $k_2(-x-h) \equiv CK_2 \exp(\beta kh(x+h/2))k_2(x)$. Replacing x by $-x-h$ gives $k_2(x) \equiv CK_2 \exp(-\beta kh(x+h/2))k_2(-x-h)$. Hence $CK_2 = 1$, and inversion symmetry for the isometric stroke rate is expressed by the identity

$$k_2(-x-h) \equiv \exp(\beta kh(x+h/2))k_2(x) \tag{1}$$

for the stroke rate $k_2(x)$. This symmetry alone is sufficient to predict the mean displacement of trap displacement experiments in the limit of perfect time resolution.

Kramers-Smoluchowski theory

For application to trap data, it is necessary to go beyond the 'highest-energy-barrier' approximation for the strain-dependent stroke rate. Specific predictions can be made from Kramers' theory of unimolecular reactions (16), using the reduction to Smoluchowski's equation which is valid in the limit of high damping (17). This approximation is appropriate for a concerted transition in a large protein.

The Kramers-Smoluchowski formula for the forward stroke rate $k_2(x)$ is

$$k_2(x) = \frac{D/Z_2(x)}{\int \exp(\beta G(x,\theta))\, d\cos\theta}, \tag{2}$$

where

$$Z_2(x) = \int_{\theta_2-\delta}^{\theta_2+\delta} \exp(-\beta G(x,\theta))\, d\cos\theta \tag{3}$$

is the partition function for the pre-stroke state, defined by a narrow angular range 2δ. D is the rotational diffusion constant of the swinging lever-arm. In this context, $Z_2(x) \approx Z_2 \exp(-\frac{1}{2}\beta kx^2)$, neglecting the variation in elastic energy over the width of the pre-stroke potential well in $G_{\mathrm{B}}(\theta)$. The integral in Eqn. 2 is dominated by the region between wells, in which the integration reduces to standard functions. Thus

$$\frac{k_2(x)}{k_2} = \frac{\tilde{h}}{e^{2\tilde{h}(\tilde{x}+\tilde{h}/2)}F(\tilde{x}+\tilde{h}) - F(\tilde{x})} \tag{4}$$

in terms of the dimensionless parameters $\tilde{x} = (\beta k/2)^{1/2} x$ and $\tilde{h} = (\beta k/2)^{1/2} h$. Here $k_2 = DR/Z_2 h$ is the stroke rate for the unloaded filament, obtained by setting k = 0, and $F(x) = \int_0^x \exp(t^2) dt$ is Dawson's integral. Inversion symmetry in the form of Eqn. 1 is satisfied because $F(x)$ is an odd function of x.

The predicted stroke rate is shown in Figure 2A, plotted against scaled strain $\tilde{x}$. The 'highest-energy-barrier' formula, in which $k_2(x)$ is constant for $x < -h/2$ and exponentially decaying with decay constant $\beta k h$ for $x > -h/2$, is approached when $\tilde{h} >> 1$. Similar statements apply to the backward rate (Figure 2B). The highest-barrier formula is an approximation, valid only to logarithmic accuracy (neglect of a power-law variation outside the exponential); Figure 2 shows that the forward rate rises linearly above k_2 as x falls below $-h/2$, and the backward rate also rises linearly above k_{-2} as x increases above $-h/2$. Thus Kramers' theory provides improved stroke-rate formulae for trap experiments ($\tilde{h} < 1.0$) and the muscle fibre ($\tilde{h} \approx 5$).

Kramers' theory predicts that $k_2 \approx 10^4 \mathrm{s}^{-1}$ if $D = 10^6 \mathrm{s}^{-1}$, $R = h = 10\mathrm{nm}$ and $Z_2 = \exp(-\beta B_2)$ with $B_2 = 20\mathrm{pN.nm}$. D is obtained via Einstein's relation from the rotational damping constant of the swinging lever-arm in solution, for which crude estimates can be made (18). The quantity B_2 is the depth of the pre-stroke energy well in $G_B(\theta)$, which is probed by the temperature dependence of the stroke rate. The above value of B_2 gives $Q_{10} = 1.8$ for the fractional rise in rate over 10^oC, which is similar to values observed in fibres (19). Thus the model can account numerically for the expected stroke rate.

MYOSIN KINETICS FOR A WEAKLY-TRAPPED FILAMENT

In the last section, strain-dependent reaction rates for the actomyosin working stroke were derived under isometric conditions. If the actin filament is moving relative to myosin, strain-dependent transition rates are smoothed in a way which depends on the extent and speed of motion. In particular, we wish to calculate effective transitions rates for a weakly-trapped actin filament, as in optical-trap experiments. It is sufficient to consider the actin-binding and working-stroke transitions. Suppose that the actin-binding constant $K_1(x)$, and the equilibrium constant $K_2(x)$ and rate constant $k_2(x)$ of the working stroke, are known functions of x for a fixed filament (the isometric case). We now show that the corresponding quantities $\bar{K}_1(x)$, $\bar{K}_2(x)$ and $\bar{k}_2(x)$ for a weakly-trapped filament undergoing rapid Brownian motion are obtained by replacing myosin stiffness k by the stiffness $\kappa \equiv k\kappa_t/(k+\kappa_t)$ of myosin and traps acting in series.

For binding to actin, let $k_1(x,u)$ and $k_{-1}(x,u)$ be the rate constants for a given initial filament displacement u (in opposition to x). The elastic energies in states 1 and 2 of Scheme 1 are respectively $\frac{1}{2}\kappa_t u^2$ and $\frac{1}{2}\kappa_t u^2 + \frac{1}{2}k(x-u)^2 \equiv \frac{1}{2}(k+\kappa_t)(u-U_2(x))^2 + \frac{1}{2}\kappa x^2$. In state 2, $U_2(x) = kx/(k+\kappa_t)$ is the mean displacement and myosin and the traps act in parallel. Averaging over the corresponding Boltzmann distributions gives

$$\bar{k}_1(x) = \left(\frac{\beta\kappa_t}{2\pi}\right)^{1/2} \int k_1(x,u)\, e^{-\frac{1}{2}\beta\kappa_t u^2}\, du, \qquad (5)$$

$$\bar{k}_{-1}(x) = \left(\frac{\beta(k+\kappa_t)}{2\pi} \right)^{1/2} \int k_{-1}(x,u)\, e^{-\frac{1}{2}\beta(k+\kappa_t)(u-U_2(x))^2}\, du. \tag{6}$$

Detailed balancing says that $k_1(x,u)/k_{-1}(x,u) \equiv K_1 \exp(-\frac{1}{2}\beta k(x-u)^2)$ where K_1 is the strain-free affinity. Hence

$$\bar{K}_1(x) \equiv \frac{\bar{k}_1(x)}{\bar{k}_{-1}(x)} = \left(\frac{\kappa_t}{k+\kappa_t} \right)^{1/2} K_1 \exp(-\tfrac{1}{2}\beta\kappa x^2). \tag{7}$$

The same line of reasoning, with the appropriate Boltzmann factor for state 3 with mean displacement $U_3(x) = k(x+h)/(k+\kappa_t)$, can be used to establish the Brownian-averaged equilibrium constant of the working stroke, namely

$$\bar{K}_2(x) \equiv K_2 \exp(-\beta\kappa h(x + h/2)). \tag{8}$$

The stated rule for generating $\bar{k}_2(x)$ from $k_2(x)$ can be demonstrated within the flat-landscape model, provided that filament Brownian motion is faster than the stroke rate. Then the distribution of displacement fluctuations equilibrates to a Boltzmann distribution at each stage of the stroke reaction. A formal method for motional averaging is Gardiner's adiabatic elimination procedure (20), which replaces the strain energy $V(x,u,\theta) \equiv \frac{1}{2}k\{x-u+R(\cos\theta-\cos\theta_2)\}^2 + \frac{1}{2}\kappa_t u^2$ of myosin and traps with the average potential

$$\begin{aligned} \bar{V}(x,\theta) &= -\beta^{-1} \ln \int e^{-\beta V(x,u,\theta)} du \\ &= \tfrac{1}{2}\kappa(x + R(\cos\theta - \cos\theta_2))^2 + \text{constant}, \end{aligned} \tag{9}$$

the constant being proportional to $k_B T$. The first term in this equation is just as for an isomeric filament, but with *k* replaced by κ. It describes the variation of strain energy along the valley floor of $V(x,u,\theta)$ as a function of *u* and θ (Figure 3), which follows the pathway $u = U(x,\theta) = k\{x + R(\cos\theta - \cos\theta_2)\}/(k+\kappa_t)$.

Figure 2 shows that under trap conditions ($\kappa = 0.02$-0.08pN/nm, $\tilde{h} = 0.5$-1.0), the strain-dependence of the stroke rate is much smoother than in the muscle fibre ($k = 1$-3 pN/nm, $\tilde{h} = 4$-6), even after scaling the pre-stroke strain *x* to its dimensionless form. Thus the high-barrier formula is simply not applicable to the weakly-trapped actin filament.

Our analysis requires that the corner frequency of Brownian filament motion with myosin bound is faster than the rates of detachment and stroking. The upper roll-off frequency of the noise spectrum is $\lambda = (k+\kappa_t)/\zeta$ (radians/s) where ζ is the viscous drag coefficient of the actin-beads assembly. Thus $\lambda = 8X10^4 \text{s}^{-1}$ for two 1μm-diameter beads, $k = 2$ pN/nm and weak traps. This frequency is higher than the values of k_{-1}, k_2 and k_{-2} used in the last section, justifying the assumption of rapid Brownian motion.

HIGH-FREQUENCY TRAP DATA

We now seek to show how the strain-dependent stroke rate $k_2(x)$ might be studied experimentally from high-frequency optical-trap displacement data (minimum resolving time $\leq 1\,\mathrm{ms}$, such that most post-stroke events present in the data are detected). In this limit, modelling shows that the mean displacement is sensitive to the kinetics of the stroke and the initial binding event. Hence more diagnostic tools are needed to characterize experimental records. More information can be obtained by working with event-averaged and time-averaged mean displacements in bound periods: experimentally, both kinds of averages can be calculated after detection of binding events.

To demonstrate sensitivity to the functional form of $k_2(x)$, we use two alternatives to the flat-landscape model (Scenario I). Length-step data in muscle fibres is qualitatively consistent with the formula $k_2(x) = k_2 \exp(-\beta k h(x + h/2))$ for all *x*, so that the rate of stroke-reversal is strain-independent (Scenario II). Finally, suppose that $k_2(x)$ is independent of x (Scenario III), so that myosin strokes with equal probability on all binding sites. These alternatives are generated by reaction-energy landscapes which differ from the flat-landscape model (Figure 1); scenario II requires a large repulsive barrier protecting the post-stroke state even at negative strains, and scenario III a similar repulsive barrier for the pre-stroke state. Such barriers would drastically alter the kinetics of the stroke transition on detached myosin.

We now discuss the interpretation and analysis of low-frequency and high-frequency trap data in terms of Scheme 1, with *x*-dependent rate constants replaced by their Brownian averages. Assuming that only post-stroke states are detected, the event-averaged and time-averaged bound-state displacements defined in the introduction are given by the expressions

$$U_{\mathrm{E}} = \frac{\int (x+h) J_3(x)\,dx}{\int J_3(x)\,dx}, \qquad U_{\mathrm{T}} = \frac{\int (x+h)\, p_{34}(x)\,dx}{\int p_{34}(x)\,dx} \tag{10}$$

where $J_3(x) = \bar{k}_2(x) p_2(x)$ is the flux into state 3 and $p_{34}(x)$ is the probability of the post-stroke states. These formulae apply to high-resolution trap data, such that all arrivals in the first post-stroke state 3 are detected. The ratios U_{E}/h and U_{T}/h are deflation factors. Simple formula can be obtained in the limit in which all transitions are in equilibrium, as expected in the complete absence of ATP; these results are a useful starting point for understanding the behaviour predicted under cycling conditions.

The equilibrium limit

Setting g = 0 gives state populations in equilibrium, such that $p_2(x) = \bar{K}_1(x) p_1$ and so on. Then $J_3(x) = \bar{k}_2(x)\bar{K}_1(x) p_1$, which is proportional to $\exp(-\frac{1}{2}\beta\kappa(x+h)^2)$ for scenario II and $\exp(-\frac{1}{2}\beta\kappa x^2)$ for scenario III (Figure 4). These forms give event-averaged displacements $U_{\mathrm{E}} = 0$ and $U_{\mathrm{E}} = h$ respectively. The flat-landscape model (scenario I) gives $U_{\mathrm{E}} = h/2$, regardless of the way in which the kinetics is derived. This somewhat magical result is a consequence of inversion symmetry. Eqn. 1 (with k replaced by κ) and Eqn. 7 imply that $J_3(-x-h) = J_3(x)$; thus the entry rate is an even function about the point $x = -h/2$ where states 2 and 3 have the same strain energy (Figure 4). If trap experiments could be made under these conditions, a mean displacement of 5-6 nm would indeed correspond to the 10-12nm working stroke required by the crystal structures.

In equilibrium, the time-averaged displacement is zero; no mechanical work is obtained as expected from thermodynamics. To check, note that $p_{34}(x) \propto \exp(-\frac{1}{2}\beta\kappa(x+h)^2)$ independently of any kinetic scenarios.

Steady-state cycling

Previous calculations for low-resolution trap data were made with Scheme 1, assuming that only state 4 could be detected (5). They showed that the irreversibility of the post-stroke product-release transitions was sufficient to drive the binding step out of equilibrium even at micromolar levels of ATP. Hence the equilibrium results are not expected to apply under the conditions commonly used for trap experiments with ATP. The state probabilities under steady-state cycling can be expressed in terms of pseudo-equilibrium constants $\bar{k}_1(x)/(k_{-1}+g_2(x))$, $\bar{k}_2(x)/(\bar{k}_{-2}(x)+g_3)$ and $k_3/(k_{-3}+g)$ respectively, where $g_2(x)=\bar{k}_2(x)g_3/(\bar{k}_{-2}(x)+g_3)$ and $g_3=k_3 g/(k_{-3}+g)$. From these expressions, the two kinds of mean displacement can be calculated in terms of the kinetic parameters and the dimensionless working stroke $\tilde{h} \equiv (\beta\kappa/2)^{1/2} h$.

The deflation factors were calculated with parameter-values about the standard set $k_{-1}=1000\,\mathrm{s}^{-1}$, $k_{-2}=250\,\mathrm{s}^{-1}$, $K_2=20$, $k_3=75\,\mathrm{s}^{-1}$, $k_{-3}=0.05\,\mathrm{s}^{-1}$, $g=10\,\mathrm{s}^{-1}$ and $\tilde{h}=1.0$ used in (5). Fibre experiments with M.ATPγS give $k_{-1} \sim 400\,\mathrm{s}^{-1}$ (21), and values of 10-40 for K_2 can be estimated from length-step data (15). The value of k_3 is obtained from a stopped-flow experiment (22), which shows that myosin achieves rapid equilibrium with actin and that phosphate release is the rate-limiting post-stroke transition to rigor. As the stroke transition is close to equilibrium ($k_{-2} >> k_3$), hence $k_{-1} > K_2 k_3$ which suggests that $k_{-1} > 1000\,\mathrm{s}^{-1}$ in solution. The above value of k_{-3} applies for 1mM Pi and micromolar levels of ADP, and g is for 5μM ATP (7). Figure 5 shows the transition from equilibrium to irreversible cycling as a function of g, which is proportional to [ATP]. The equilibrium results are recovered in the limit $g << k_{-3}$, which requires subnanomolar ATP concentrations. However, the lifetime K_2/k_{-3} of state 4 would then be about $400\,\mathrm{s}^{-1}$, requiring excessively long experimental records. In the opposite limit $g >> k_{-3}$, the post-stroke transitions are irreversible and the deflation factors approach asymptotic values. Here the event-averaged deflation factors vary significantly with the kinetic model of the working stroke, namely 0.82, 0.52 and 1.23 for scenarios I, II and III respectively. However, the time-averaged factors for the three scenarios are very similar and cluster around 0.5. For scenario II, event-averaged and time-averaged deflation factors are identical, because the rate $k_{-2}(x)$ of stroke reversal which affects the lifetime of state 3 is independent of x.

At high time resolution, the deflation factors also vary with the size of the stroke and the stiffness of the traps, through the dimensionless stroke as shown in Figure 6. As described previously for low resolution data, the amount of deflation is sensitive to the detachment rate k_{-1} and the stroke equilibrium constant K_2. These variations are shown in Figure 7. In spite of these uncertainties, the major result of this modelling exercise is that event-averaged and time-averaged displacements for high-frequency data are generally different. Also, both quantities are slowly decreasing function of trap stiffness and resolving time, variables which are under experimental control. Both effects are a function of the strain-dependent kinetics of the stroke rate. In this way, it may be possible to test the different scenarios proposed here by optical-trap experiments.

THE EFFECTS OF FINITE TIME RESOLUTION

The time resolution of detected attachment events in current trap displacement data (sampling frequency ~ 10KHz) is currently limited by the need to construct a running variance record (6,7), and is typically about 5ms. In this interval, the myosin may escape from state 3 by a reverse stroke at about $250\,\mathrm{s}^{-1}$, rather than by release of phosphate and ADP. We now generalize the previous treatment of Scheme 1 to data in which events have been detected with an arbitrary resolving time s. In the process, the previous results obtained with event-averaging (5) are recovered when $s \geq 5\,\mathrm{ms}$.

For a given resolving time, exact formulae can be obtained in terms of the probability $P_{34}(x,t)$ that myosin arriving in state 3 survives in either state 3 or state 4 over time t. This object can be calculated from modified rate equations for these states, in which $k_2(x)$ is set equal to zero (23). The required solution is

$$P_{34}(x,t) = \sum_{\pm} a_{\pm}(x) \exp(-\lambda_{\pm}(x)t) \tag{11}$$

where

$$\lambda_{\pm}(x) = \tfrac{1}{2}\left\{ \begin{array}{l} \bar{k}_{-2}(x) + k_3 + k_{-3} + g \\ \quad \pm \sqrt{(\bar{k}_{-2}(x) + k_3 - k_{-3} - g)^2 + 4k_3 k_{-3}} \end{array} \right\} \tag{12}$$

and

$$a_{\pm}(x) = \pm \frac{\lambda_{\pm}(x) - k_3 + k_{-3} - g}{\lambda_{+}(x) - \lambda_{-}(x)}. \tag{13}$$

For event-averaging, we require the frequency of detected events at time resolution s, which is obtained by inserting the filtering function $P_{34}(x,s)$. For time averaging, each detected event must be weighted with its lifetime, which must exceed the resolving time. The mean lifetime is

$$\tau_{34}(x,s) = \frac{\int_s^{\infty} t\rho_{34}(x,t)dt}{\int_s^{\infty} \rho_{34}(x,t)dt} \tag{14}$$

where $\rho_{34}(x,t) = -\partial P_{34}(x,t)/\partial t$ is the distribution of the lifetime t. Hence

$$\tau_{34}(x,s) = s + \frac{\sum_{\pm} \lambda_{\pm}(x)^{-1} a_{\pm}(x) \exp(-\lambda_{\pm}(x)s)}{\sum_{\pm} a_{\pm}(x) \exp(-\lambda_{\pm}(x)s)}. \tag{15}$$

Thus event-averaged and time-averaged displacements at finite time-resolution are given by Eqn. 10 with $J_3(x)$ and $p_{34}(x)$ replaced by their filtered counterparts

$$J_3^{(\mathrm{F})}(x,s) \equiv J_3(x)P_{34}(x,s), \tag{16a}$$

$$p_{34}^{(\mathrm{F})}(x,s) \equiv J_3(x)P_{34}(x,s)\tau_{34}(x,s). \tag{16b}$$

When s = 0, the right-hand side of Eqn. 16a reduces to $J_3(x)$ and that of Eqn. 16b to an expression proportional to $p_{34}(x)$. These formulae were used to calculate both deflation factors as a function of resolving time (Figure 8). The results of the previous section for high-frequency data, which discriminate between the three stroke-rate scenarios and between event-averaging and time-averaging, are reproduced when s = 0, and approximately so when $s \le 1\,\mathrm{ms}$. The low-frequency limit is achieved when $s \ge 5\,\mathrm{ms}$; in this case, the three stroke-rate scenarios give almost identical results and there is no difference between event-averaged and time-averaged displacements. The critical resolving time s_* separating high-frequency and low-frequency data is estimated by $(k_{-2} + k_3)s_* = 1$; for the standard parameter set, $s_* = 3\,\mathrm{ms}$.

For low-frequency data, the above predictions correspond to those obtained by assuming that only state 4 could be detected (5). The two methods of calculation are not mathematically equivalent, but closely related for realistic values of kinetic parameters. To demonstrate this relationship, we simplify Eqns. 12-13 by setting $k_{-3} = 0$, a limit which can be taken when $g >> k_{-3}$. The eigenvalues in Eqn. 12 are then the lifetimes of states 3 and 4: $\lambda_+(x) = \bar{k}_{-2}(x) + k_3$ and $\lambda_-(x) = g$. As s increases from zero, the filtering function $P_{34}(x,s)$ drops from unity to a plateau of height $k_3/(\bar{k}_{-2}(x) + k_3)$ in a range of resolving times such that $s_* << s < g^{-1}$, which defines the range of low-frequency data. This range exists if $k_{-2} + k_3 >> g$, which is satisfied experimentally. Then $J_{3F}(x) \cong J_4(x)$, the rate $k_3 p_3(x)$ of entry to state 4, which validates the simpler approach used in (5) to calculate the event-averaged displacement.

Time-averaging of low-frequency data gives the same mean displacement as event-averaging, because the mean lifetime $\tau_{34}(x,s)$ reduces to $s + g^{-1}$, which is independent of x. This result can also be understood in terms of the previous treatment which assumed that only state 4 could be detected. In that case, $J_4(x) = k_3 p_3(x)$ is proportional to $p_4(x)$ because the ratio $p_4(x)/p_3(x) = k_3/(k_{-3} + g)$ is also x-independent.

DISCUSSION

Testing different scenarios for the stroke rate

The true strain-dependence of the stroke rate of bound myosin can be tested through experiments on the muscle fibre or on a single myosin-S1. With intact fibres, length-step experiments rule out scenario III ($k_2(x)$ constant) and can in principle discriminate between scenarios I (flat-landscape model) and II ($k_{-2}(x)$ constant) through the variation of the rate of phase-2 tension recovery on the size of the release step (15). In practice, the differences would appear only for large releases ($> 5\,\mathrm{nm}$) and may be obscured by experimental artifacts.

For single-myosin displacement data from weak-trap experiments with ATP, our predictions for the three scenarios of the strain-dependent stroke rate are summarized in Figures 6-8. The different scenarios are manifest only in high-frequency data, where the minimum resolving time is under 1ms; in this limit the event-averaged displacement during bound periods is much more sensitive than the time-averaged displacement to the details of stroke kinetics (Figure 7). This occurs because the three scenarios affect averaged displacements through their effect on the strain-dependence of the stroke rate, which affects the populations of post-stroke states on different actin sites. Complementary effects on the rate of the backward stroke may generate strain-dependent lifetimes for these states, which

generate numerical differences between event-averaged and time-averaged displacements in bound periods. Such experiments could also confirm that myosin exists in a post-stroke state during the observed bound periods.

Consider three aspects of the problem from an operational standpoint. How could we tell that a particular data-set lies in the high-frequency range? What method of analysis would best reveal which stroke-rate scenario fits the data? How can such measurements provide estimates for the myosin working stroke, given that both kinds of deflation factor (mean displacement/working stroke) are still sensitive to the parameters of the model?

The first question is addressed by noting that high-frequency data should display some correlation between the displacements and the lifetimes of (post-stroke) bound states. This information could be obtained from a scatter plot which would reflect fluctuations in the mean displacement and Poisson fluctuations in the lifetime of each bound period in the data. No such correlation has been observed in existing data (minimum resolving time ~ 5ms) from the trap group at King's College London. The scale of the effect to be expected can be judged from Figure 9, which presents the variation of the mean lifetime of the post-stroke states 3 and 4 as a function of displacement/working stroke; there is a large variation of lifetime with displacement for scenarios I and III, but none for scenario II. However, the range of observed displacements is proscribed by the population curves in Figure 4, which have a half-width of about unity in the ordinate; thus a five-fold variation in mean lifetime could be expected from the scatter diagram if scenarios I or III apply. This procedure should provide a simple test of stroke kinetics from high-frequency data.

If the data is thought to be of sufficient time resolution, we then require analyses which discriminate between these scenarios, given that the size of the stroke cannot easily be extracted from the data. For example, event-averaged displacements could be measured over a wide range of values of trap stiffness; the event-averaged deflation factor (Figure 6A) increases according to the amount of strain-dependence assigned to the rate of the reverse stroke. More information is obtained from the ratio of event-averaged and time-averaged displacements, which is also the ratio of the deflation factors. For time-averaging, the deflation factor for all stroke scenarios is close to 0.5 (Figure 6B), so that the ratio of event-averaged to time-averaged deflation factors at very low trap stiffness ($\tilde{h} = 0.1$) is approximately 2, 1 and 3 for scenarios I,II and III. Exact ratios can be obtained from the figures for higher values of $\tilde{h}$. Lastly, high-frequency displacement-time records can be analysed over a range of resolving times for event detection. Figure 8A shows that these values are reproduced by the ratio of event-averaged displacements at high and low time resolution, since the corresponding deflation factors of all scenarios are the same in the low-resolution limit.

In practice, these methods should not be regarded as exact, because the predicted deflation factors vary significantly with the kinetic parameters k_{-1}, k_2, k_{-2} and k_3 (see Figure 7). However, the ratio of event-averaged and time-averaged factors shows much less variation (Figure 7C) and should therefore be used in preference when values of the associated parameters are not known.

Estimating the working stroke from trap experiments

Do these methods of analysis help us to estimate the myosin working stroke from high-frequency trap displacement data? At first glance, we appear to be in the same situation pertaining to low-frequency data (5); both kinds of mean displacement are predicted to vary widely with kinetic parameters. The ability to measure two kinds of mean displacements as functions of trap stiffness and time resolution might permit a global fit to the model as a function of k_{-1} and k_2, particularly if the kinetics of the working stroke is known.

Related considerations

Our predictions are tied to a particular model of actin-myosin kinetics, which includes the assumption that no second stroke is associated with ADP release. Until recently (24), there has been no substantive evidence for a second stroke in myosin II. If a second stroke of 1-2 nm does occur after Pi release, its strain-dependent kinetics should be largely washed out by Brownian averaging, and the predictions of our current model should be qualitatively correct apart from the different mean displacements associated with states before and after the second stroke. The model could easily be amended in this way.

The model also applies to trap displacement data under conditions where no ATP is present. In the absence of an energy source, the data should sample attachment events under conditions of thermodynamic equilibrium and the time-averaged displacement should be zero. The equilibrium case of the model discussed in section three predicts non-zero event-averaged displacements of $h/2$ and h for scenarios I and III respectively and high-frequency data, where all post-stroke states are detected. In this case, the event-averaged displacement is indifferent to the presence of the phosphate-release step after the working stroke, and the same results hold at any time resolution for a three-state model defined just by binding and stroking transitions. Previous observations of zero mean displacement for myosin complexed with various non-hydrolysable nucleotide analogues (AMPPNP, ATPγS, PPi) can be assessed in the light of these predictions, without changing the conclusions drawn (25). If these complexes did make a working stroke after actin-binding and scenario I applies as expected, then the size of the stroke must have been less than 2 nm. Most of these complexes are thought to have an open nucleotide pocket, for which the lever arm is in a post-stroke configuration; thus these complexes bind without changing the orientation of their lever arm. A complete discussion is given in the original paper.

Finally, note that none of the above analysis would be necessary if the pre-stroke state could be detected directly in trap experiments. The inverse lifetime of the strained pre-stroke state is $\bar{k}_2(x)+k_{-1}$, which varies from k_{-1} at large positive x to values in excess of k_2+k_{-1} at large negative x (Figure 2). Thus resolution times of 0.1 ms or less would be required to see this state on all sites. There are two possible developments which might allow detection of sub-millisecond events. One is to use considerably smaller beads (diameter < 0.2 μm), so that the corner frequency (the upper roll-off of the power spectrum of Brownian filament motion) is raised to the required value. Single-bead experiments are being carried out on kinesin with beads of this size (26), but dumbbell experiments present extra problems to be solved to facilitate experiments with such small beads. If changes in the variance of bead position are to be used to detect attachment events on a millisecond time scale, then the corner frequency of the trapped bead must be raised by a combination of smaller beads and stiffer traps. An alternative approach is to detect binding events directly from the position-time records of the beads, rather than from constructed running- variance records. This approach requires that the relative positions of the free dumbbell and the myosin-bearing fixed bead remain constant at the level of 1nm for the duration of the experiment, and is a realistic goal for the near future.

Acknowledgements: D.A.S. acknowledges financial support from NIH grant no. R01 AR048776-01A1 and J.S. from the Medical Research Council. We wish to thank Dr. Justin Molloy and Prof. Robert Simmons for comments on an earlier version of this paper.

REFERENCES

1. Huxley, A.F. and R.M. Simmons. 1971. Proposed mechanism of force generation in striated muscle. *Nature* 233, 533-538.
2. Rayment, I., H.M. Holden, M. Whittaker, C.B. Yohn, M. Lorenz, K.C. Holmes and R.A. Milligan. 1993. Structure of the actin-myosin complex and its implications for muscle contraction. *Science* 261, 58-65.
3. Houdusse, A., A.G. Szent-Gyorgi and C. Cohen. 2000. Three conformational states of scallop myosin S1. *Proc. Nat. Acad. Sci. USA* 97, 11238-11243.
4. Taylor, K.A., H. Schmitz, M.C. Reedy, Y.E. Goldman, C. Franzini-Armstrong, H. Sasaki, R.T. Tregear, K. Poole, C. Lucaveche, R.J. Edwards, L.F. Chen, H. Winkler and M.K. Reedy. 1999. Tomographic 3D reconstruction of quick-frozen, Ca2+ activated contracting insect flight muscle. *Cell* 99, 421-431.
5. Sleep, J., A. Lewalle and D.A. Smith. 2006. Reconciling the working strokes of a single head of skeletal myosin estimated from laser-trap experiments and crystal structures. *Proc. Nat. Acad. Sci. USA* 103, 1278-1282.
6. Molloy, J.E., J.E. Burns, J. Kendrick-Jones, R.T. Tregear and D.C.S. White. 1995. Movement and force produced by a single myosin head. *Nature* 378, 209-212.
7. Smith, D.A., W. Steffen, R.M. Simmons and J. Sleep. 2001. Hidden-Markov methods for the analysis of single-molecule actomyosin displacement data: The Variance Hidden-Markov method. *Biophys. J.* 81, 2795-2816.
8. Ford, L.E., A.F. Huxley and R.M. Simmons. 1977. Tension responses to sudden length change in stimulated frog muscle fibres near slack length. *J. Physiol. (London)* 269, 441-515.
9. Baker, J.E., L.E.W. LaConte, I. Brust-Macher and D.D. Thomas. 1999. Mechanochemical coupling in spin-labelled, active, isometric muscle. *Biophys. J.* 77, 2657-2664.
10. Hopkins, S.C., C. Sabido-David, J.E.T. Corrie, M. Irving and Y.E. Goldman. 1998. Fluoresence polarization transients from rhodamine isomers on the myosin regulatory light chain in skeletal muscle fibres. *Biophys. J.* 74, 3093-3110.
11. Fischer, S., B. Windschugel, D. Horak, K.C. Holmes and J.C. Smith. 2005. Structural mechanism of the recovery stroke of the myosin molecular motor. *Proc. Nat. Acad. Sci. USA* 102, 6873-6878.
12. Dobbie, I., M. Linari, G. Piazzesi, M. Reconditi, N. Koubassova, M.A. Ferenczi, V. Lombardi and M. Irving. 1998. Elastic bending and active tilting of myosin heads during muscle contraction. *Nature* 393, 383-387.
13. Kohler, J., G. Winkler, I. Schulte, T. Scholz, W. McKenna, B. Brenner and T. Kraft. 2002. Mutation of the myosin converter domain alters cross-bridge elasticity. *Proc. Nat. Acad. Sci. USA* 99, 3557-3562.
14. Piazzesi, G. and V. Lombardi. 1995. A cross-bridge model that is able to explain mechanical and energetic properties of shortening muscle. *Biophys. J.* 68, 1966-1979.
15. Smith, D.A. and J. Sleep. 2004. Mechanokinetics of rapid tension recovery in muscle: the myosin working stroke is followed by a slower release of phosphate. *Biophys. J.* 87, 442-456.
16. Kramers, H.A. 1940. Brownian motion in a field of force and the diffusion model of chemical reactions. *Physica* VII, 284-304.
17. Brinkman, H.C. 1956. Brownian motion in a field of force and the diffusion model of chemical reactions II. *Physica* XXII, 149-155.
18. Happel, J. and H. Brenner. 1983. *Low Reynolds Number Hydrodynamics* (Martinus-Nijhoff, The Hague), pp 227-230.

19. Piazzesi, G., M. Reconditi, N. Koubassova, V. Decostre, M. Linari, L. Lucii and V. Lombardi. 2003. Temperature dependence of the force-generating process in single fibres from frog skeletal muscle. *J. Physiol.* 549.1, 93-106.
20. Gardiner, C.W. 1990. *Handbook of Stochastic methods for Physics, Chemistry and the Natural Sciences,* 2nd edition (Springer-Verlag, Berlin), pp 195-200.
21. Kraft, T., L.C. Yu, H.J. Kuhn and B. Brenner. 1992. Effect of Ca^{2+} on weak cross-bridge interaction with actin in the presence of adenosine 5′-[γ-thio]triphosphate. *Proc. Nat. Acad. Sci. USA* 89, 11362-11366.
22. White, H.D., B. Belknap and M.R. Webb. 1997. Kinetics of nucleoside triphosphate cleavage and phosphate release steps by associated rabbit skeletal actomyosin, measured using a novel fluorescent probe for phosphate. *Biochemistry* 36, 11828-11836.
23. Colquhoun, D. and A.G. Hawkes. 1981. On the stochastic properties of single ion channels. *Proc. Roy. Soc. London.* B211, 205-235.
24. Capitanio, M., M. Canepari, P. Cacciafesta, V. Lombardi, R. Cicchi, M. Maffei, F.S. Pavone and R. Bottinelli. 2006. Two independent mechanical events in the interaction cycle of skeletal muscle myosin with actin. *Proc. Nat. Acad. Sci. USA* 103, 87-92.
25. Steffen, W., D. Smith and J. Sleep. 2003. The working stroke on myosin-nucleotide complexes binding to actin. *Proc. Nat. Acad. Sci. USA* 100, 6434-6439.
26. Nishiyama, M., E. Muto, Y Inoue, T. Yanagida and H. Higuchi. 2001. Substeps within the 8-nm step of the ATP-ase cycle of single kinesin molecules. *Nat. Cell Biol.* 3, 425-428.

FIGURE CAPTIONS

Figure 1. Cartoons of the myosin working stroke when bound to actin, and Gibbs energies of the 'flat landscape' model as a function of lever-arm angle θ. **A**: for unloaded myosin, the lever arm swings by distance h (the working stroke) parallel to the filament, with a flat landscape $G_{\mathrm{B}}(\theta)$ between narrow potential wells at the pre-stroke and post-stroke angles θ_2, θ_3. **B**: When the distal end of the lever arm is fixed, the stroke works against the elastic energy $V(x,\theta)$ of bending the arm, and the energy landscape $G(x,\theta) = G_{\mathrm{B}}(\theta) + V(x,\theta)$ is a function of myosin-site distance x, plotted for x = 0 (unstrained before stroking), $x = -h$ (unstrained after stroking) and $x = -h/2$ (no change in strain). For clarity, strained states are depicted by distributed curvature in the lever arm. Parabolic strain-energy curves were generated with $h = 10\,\mathrm{nm}$ and $k = 1\,\mathrm{pN/nm}$. Energies are measured from the plateau.

Figure 2: Strain-dependent rate constants for the working stroke (**A**) and its reversal (**B**), predicted from the flat-landscape model using Kramers' theory in the limit of large damping (Eqn. 4), and plotted against the scaled offset-distance $\tilde{x} = (\beta k/2)^{1/2} x$. The family of curves is generated by the scaled working stroke $\tilde{h} = (\beta k/2)^{1/2} h$, in multiples of 0.5. Both rates are shown as fractions of the solution rate, obtained by setting k = 0.

Figure 3: The two-dimensional flat-landscape model for the working stroke on an elastically loaded filament, showing Gibbs energy $G(x,u,\theta) = G_{\mathrm{B}}(\theta) + V(x,u,\theta)$ (see main text) as a function of lever angle θ and filament displacement u for x = 0 (**A**) and $x = -10\,\mathrm{nm}$ (**B**). The surfaces are drawn for a load stiffness of 0.05 pN/nm, as in an optical trap, with values of h and k as in Figure 1. Arrows indicate the valley path of least energy; the highest energy barrier on this pathway is limited by the stiffness of the load and is much smaller than in Figure 1.

Figure 4: The frequency $J_3(x)$ of entry to the first post-stroke state 3 (arbitrary vertical scale) under equilibrium conditions, against filament displacement $x+h$ as a fraction of the working stroke h. Here x is the myosin-site distance along the resting filament. For scenarios I,II,III for the stroke rate $k_2(x)$, the uncorrected mean displacements are respectively $h/2$, 0 and h. For scenario I (the flat-landscape model), Eqn. 4 was used for the stroke rate, but any rate function satisfying inversion symmetry (Eqn. 1) will give the same mean displacement.

Figure 5: Deflation factors U_{E}/h and U_{T}/h (uncorrected mean displacement/working stroke) for high-resolution trap data and kinetic Scheme 1, as a function of the rate g of ATP-induced detachment from rigor. All curves were generated with standard values of the remaining parameters. Event-averaging was used in graph **A** and time-averaging in graph **B**. The former depend markedly on different scenarios for the strain-dependent stroke rate (see main text). As g increases, the extent of departure from equilibrium is determined by the rate k_{-3} of reversing the product-release transitions, steps, here set at $0.05\ \mathrm{s}^{-1}$.

Figure 6: Deflation factors (uncorrected mean displacement/working stroke) for high-resolution data, as a function of reduced stroke size $\tilde{h} \equiv (\beta\kappa/2)^{1/2} h$, using **A**: event-averaging and **B**: time-averaging. Typical values for $\tilde{h}$ in trap experiments lie between 0.5 and 1.0. In this region, the event-averaged factor is particularly sensitive to the different stroke-rate scenarios I,II,III.

Figure 7: Deflation factors for high-resolution trap data as a function of K_2 (strain-free equilibrium constant of the working stroke) and k_{-1} (detachment rate of the pre-stroke state), for stroke-rate scenarios I-III with **A**: event-averaging and **B**: time-averaging. Graphs **C** show the ratio of event-averaged to time-averaged deflation factors. The behaviour shown in **A** is similar to that presented in (5) for low-resolution data.

Figure 8: The effects of changing the time resolution of the event detector. **A**: event-averaged and **B**: time-averaged deflation factors move from the high-resolution limit to the low-resolution regime as the resolving time is increased through 3ms. In the low-resolution limit, event-averaged and time-averaged deflation factors are equal and agree with those predicted by assuming that only rigor states were detected (5).

Figure 9: The mean lifetime of the bound states 3 and 4 as a function of normalized mean displacement on site x for scenarios I-III, calculated from Eqn. 14 with $s = 0$ using the standard parameters of the main text. In conjunction with Figure 4, this graph is intended as a guide to scatter diagrams of experimental bound-state lifetimes versus their displacements for high-frequency trap data.

Figure 1

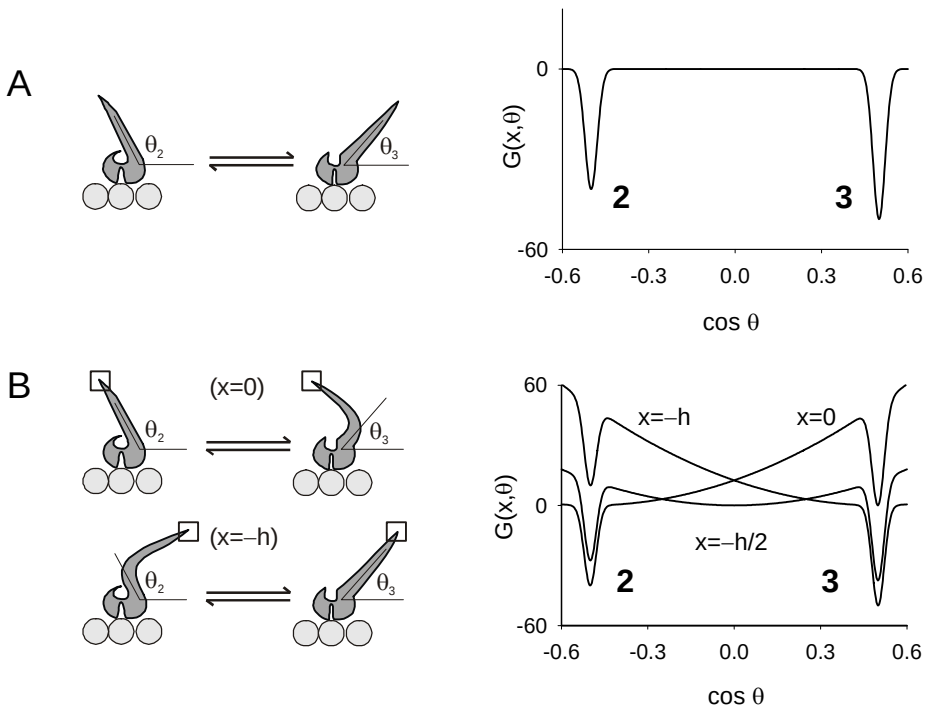
A
θ2
θ3
0
G(x,θ)
2
3
-60
-0.6
-0.3
0.0
0.3
0.6
cos θ
B
(x=0)
θ2
θ3
(x=–h)
θ2
θ3
60
x=–h
x=0
0
x=–h/2
G(x,θ)
2
3
-60
-0.6
-0.3
0.0
0.3
0.6
cos θ

Figure 2

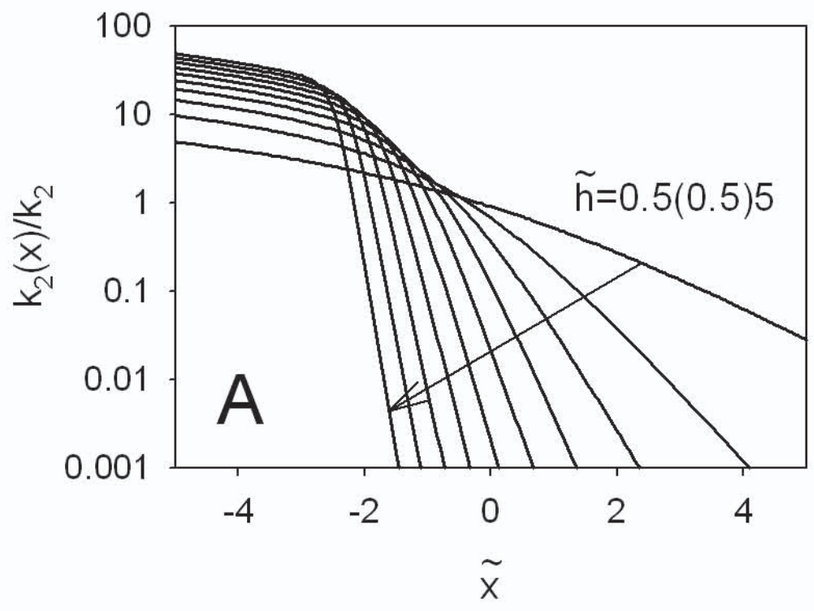
100
10
1
0.1
0.01
0.001
$k_2(x)/k_2$
A
$\tilde{h}$=0.5(0.5)5
-4
-2
0
2
4
$\tilde{x}$

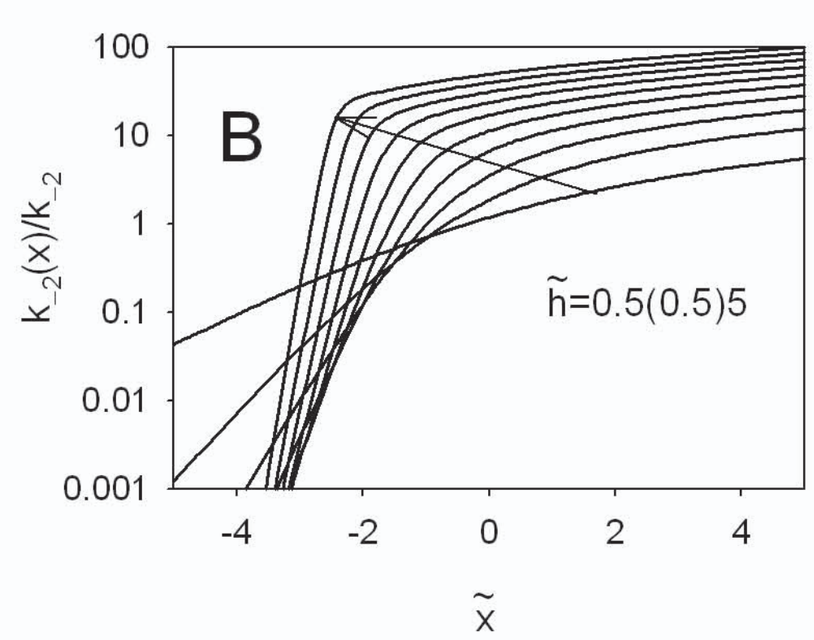
100
10
1
0.1
0.01
0.001
$k_{-2}(x)/k_{-2}$
B
$\tilde{h}$=0.5(0.5)5
-4
-2
0
2
4
$\tilde{x}$

Figure 3

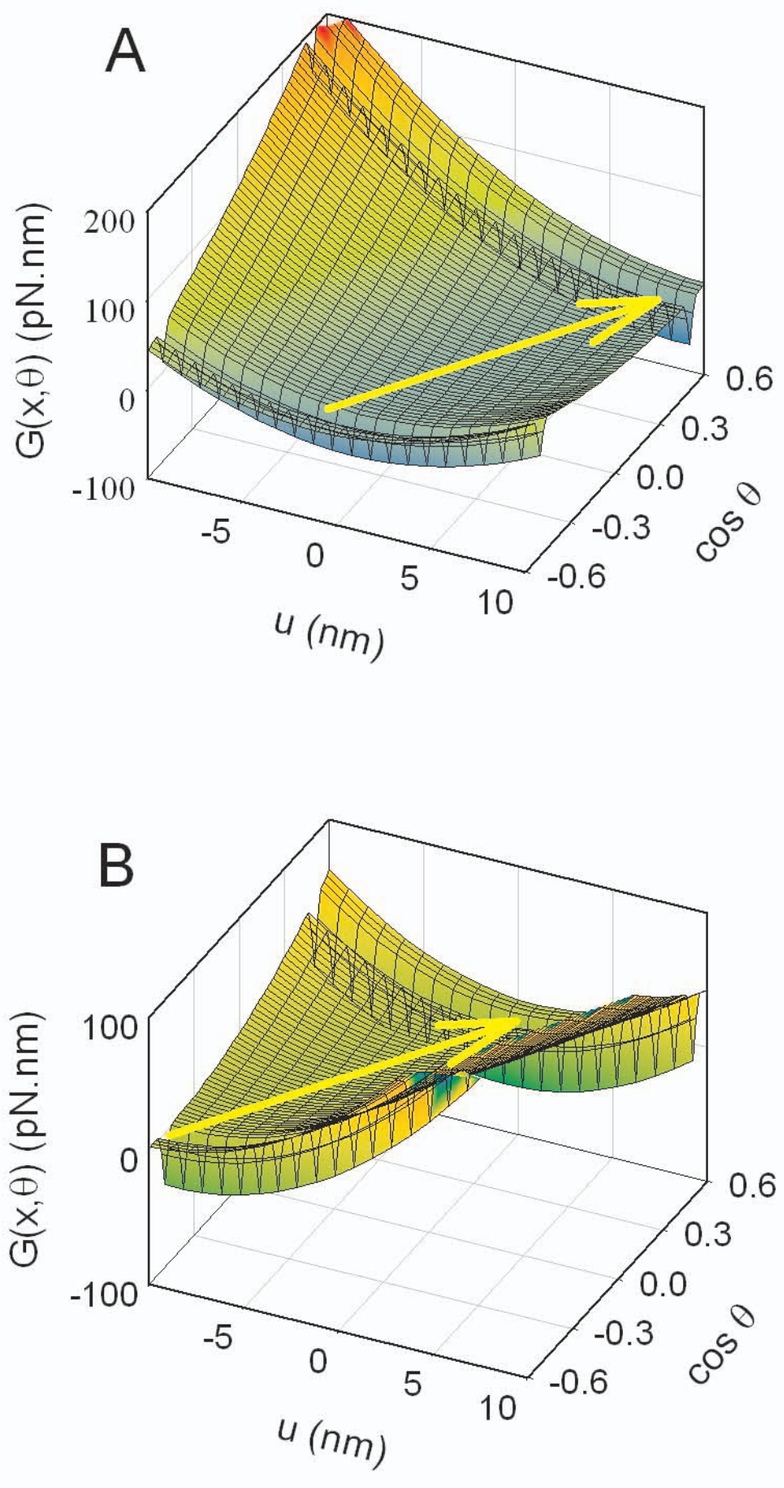

Figure 4

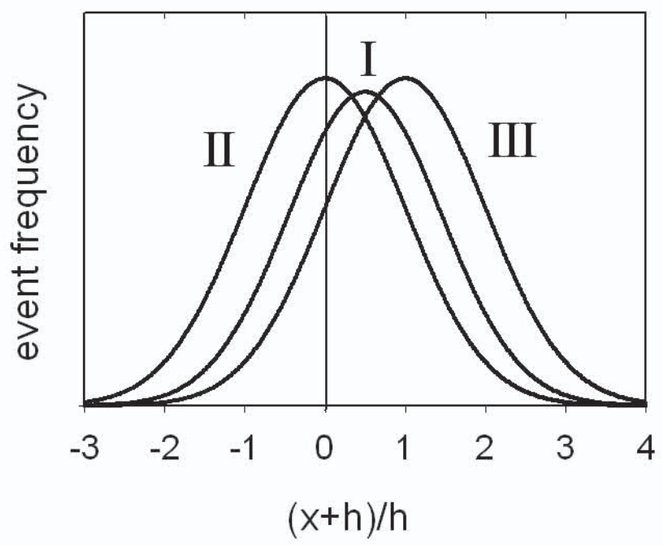

Figure 5

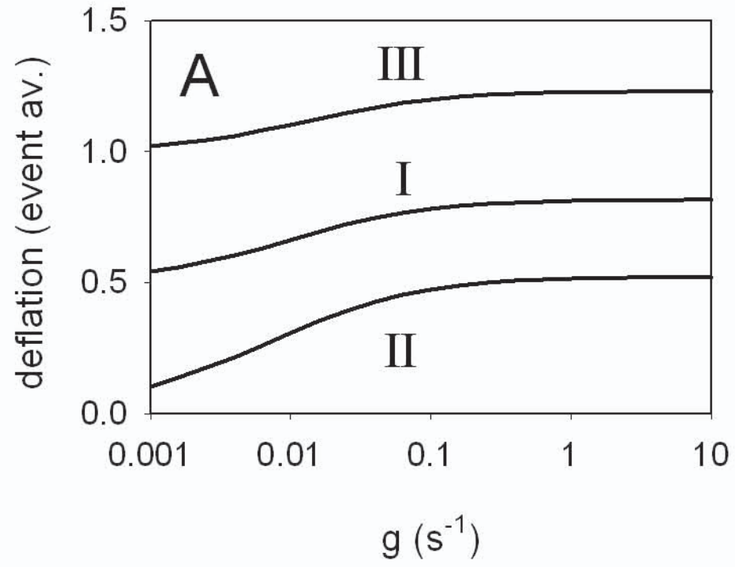
A
III
I
II
1.5
1.0
0.5
0.0
deflation (event av.)
0.001
0.01
0.1
1
10
g (s-1)

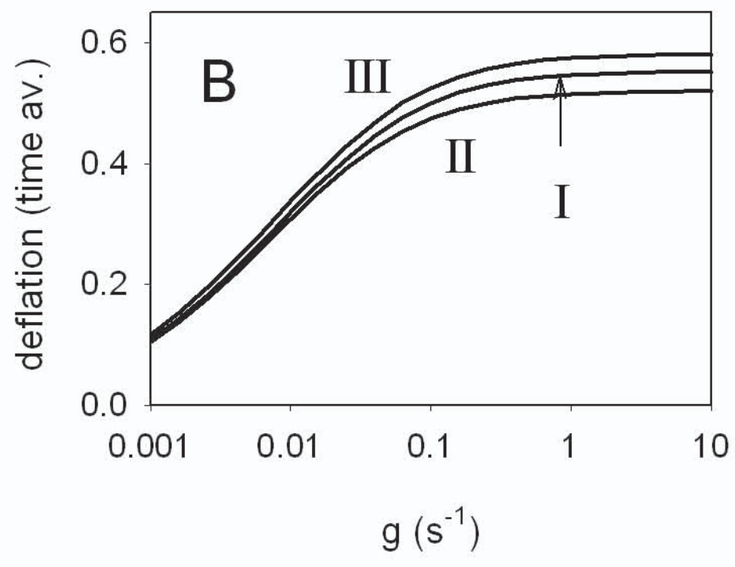
B
III
II
I
0.6
0.4
0.2
0.0
deflation (time av.)
0.001
0.01
0.1
1
10
g (s-1)

Figure 6

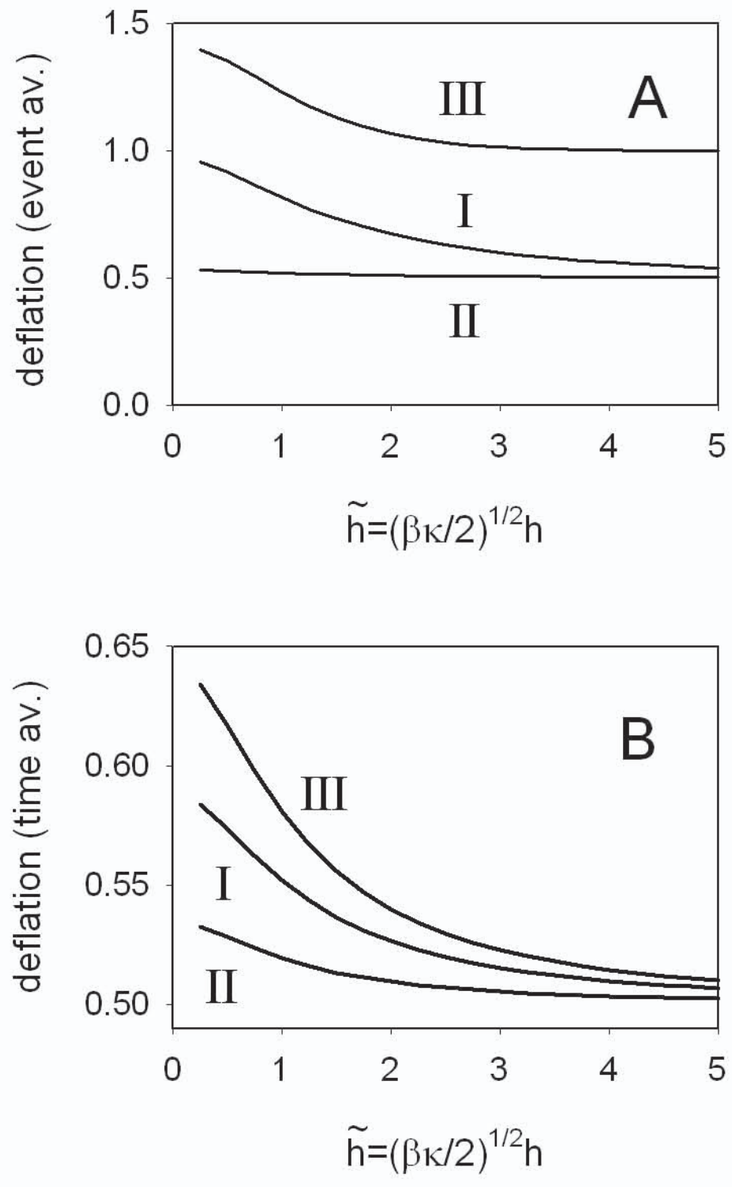
1.5
1.0
0.5
0.0
deflation (event av.)
III
A
I
II
0
1
2
3
4
5
$\tilde{h}=(\beta\kappa/2)^{1/2}h$
0.65
0.60
0.55
0.50
deflation (time av.)
B
III
I
II
0
1
2
3
4
5
$\tilde{h}=(\beta\kappa/2)^{1/2}h$

Figure 7

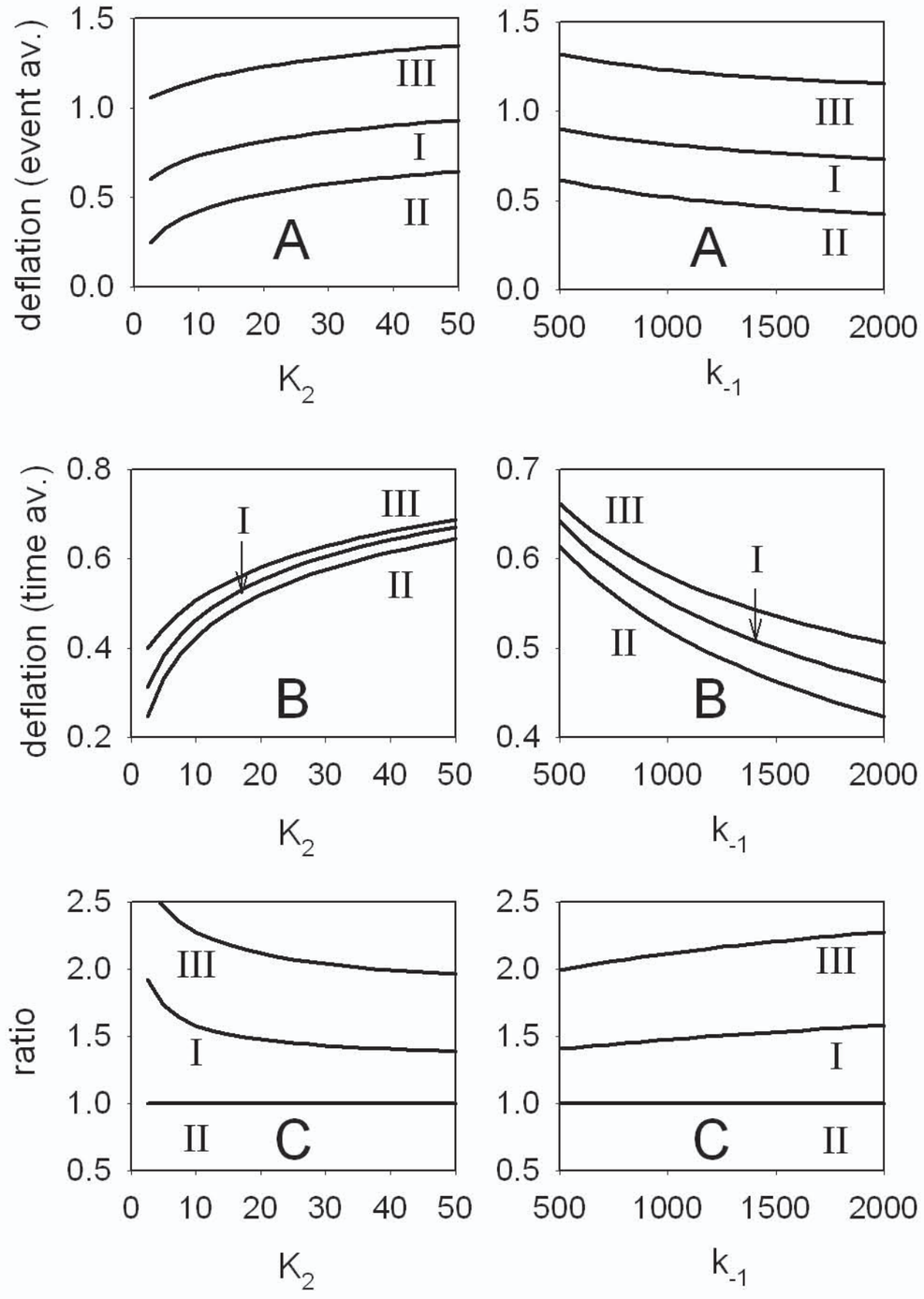
deflation (event av.)
1.5
1.0
0.5
0.0
III
I
II
A
0 10 20 30 40 50
K_2
500 1000 1500 2000
k_{-1}
deflation (time av.)
0.8
0.6
0.4
0.2
0.7
B
ratio
2.5
2.0
1.5
1.0
0.5
C

Figure 8

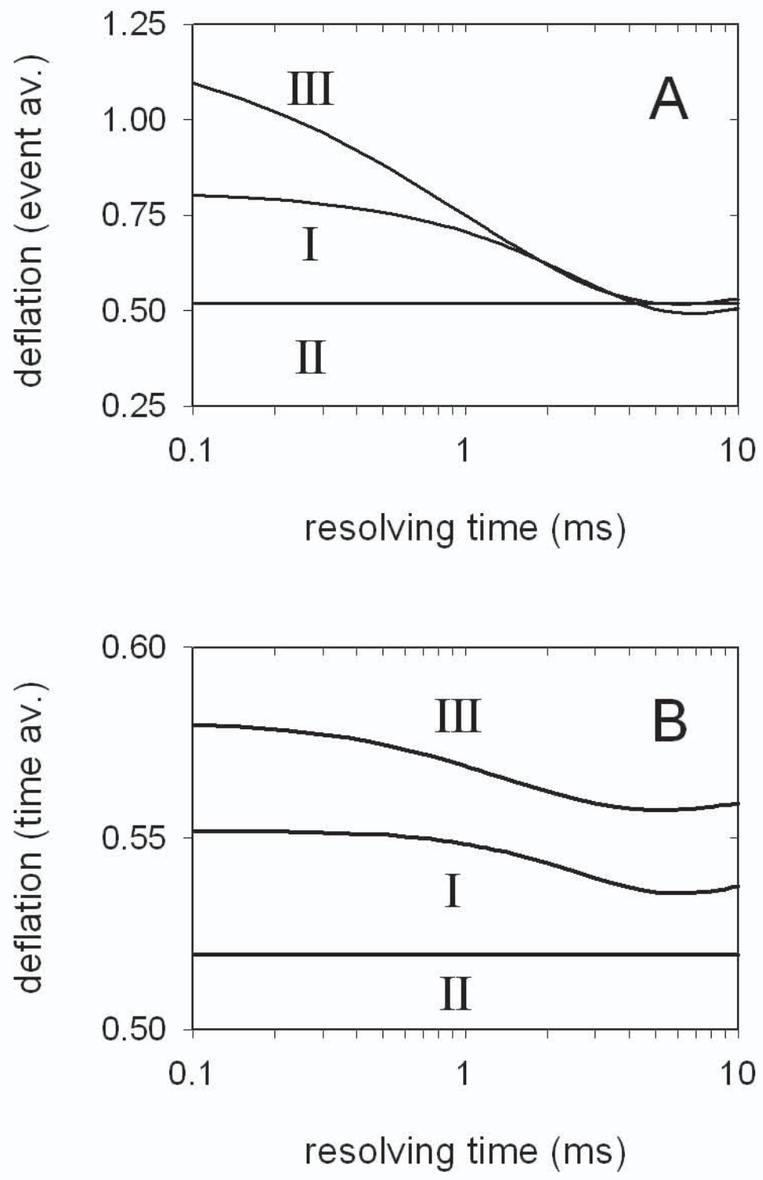
1.25
1.00
0.75
0.50
0.25
deflation (event av.)
III
I
II
A
0.1
1
10
resolving time (ms)
0.60
0.55
0.50
deflation (time av.)
III
I
II
B
0.1
1
10
resolving time (ms)

Figure 9